UC Irvine

UC Irvine Previously Published Works

Title

Multiscale wavelet decomposition of time-resolved X-ray diffraction signals in cyclohexadiene

Permalink

https://escholarship.org/uc/item/3h97w1z3

Journal

Proceedings of the National Academy of Sciences of the United States of America, 115(41)

ISSN

0027-8424

Authors

Osipov, Vladimir Al
Kowalewski, Markus
Mukamel, Shaul

Publication Date

2018-10-09

DOI

10.1073/pnas.1811983115

Copyright Information

This work is made available under the terms of a Creative Commons Attribution License, availalbe at https://creativecommons.org/licenses/by/4.0/

Peer reviewed

eScholarship.org Powered by the California Digital Library
University of California

Multiscale wavelet decomposition of time-resolved X-ray diffraction signals in cyclohexadiene

Vladimir Al. Osipov[a,b,1], Markus Kowalewski[c,1], and Shaul Mukamel[a,b,2]

[a]Department of Chemistry, University of California, Irvine, CA 92697-2025; [b]Department of Physics and Astronomy, University of California, Irvine, CA 92697-2025; and [c]Department of Physics, AlbaNova University Center, Stockholm University, 10691 Stockholm, Sweden

Contributed by Shaul Mukamel, August 17, 2018 (sent for review July 12, 2018; reviewed by Mikhail Ivanov and Hans Jakob Woerner)

We demonstrate how the wavelet transform, which is a powerful tool for compression, filtering, and scaling analysis of signals, may be used to separate large- and short-scale electron density features in X-ray diffraction patterns. Wavelets can isolate the electron density associated with delocalized bonds from the much stronger background of highly localized core electrons. The wavelet-processed signals clearly reveal the bond formation and breaking in the early steps of the photoinduced pericyclic ring opening reaction of 1,3-cyclohexadiene, which are not resolved in the bare signal.

chemical reaction movies | conical intersections | multiscale charge density analysis | ultrafast X-ray diffraction | wavelet transform

The distribution of electrons is responsible for chemical bonding as well as many other physical and chemical molecular properties. Chemical reactions can be studied in detail using femtosecond free electron laser pulses, which monitor the evolving electron density distribution. Valence bond theory complements molecular orbital theory, which adheres to the idea that electron pairs are distributed in sets of molecular orbitals delocalized across the molecule. The basic premise of density functional theory (1, 2) is that all properties of a many-electron system are uniquely determined by its electron density that depends on three space coordinates and time. Knowledge of the electron density and its time evolution is thus required for a detailed understanding of all physical and photochemical processes.

The electron density in molecules has regions of high electron density centered around the nuclei, accompanied by lower-density regions along the chemical bonds. The ground-state electron density can be measured with atomic-scale spatial resolution by X-ray diffraction. Intense femtosecond X-ray pulses allow one to carry out time-resolved X-ray diffraction from nanocrystals, as well as gas- and liquid-phase samples (3–6). Valence electrons undergo femtosecond to picosecond rearrangements which accompany the geometrical changes during chemical reactions. Stroboscopic measurements of the valence electron redistribution allow the monitoring of ultrafast electronic processes and reaction paths. The scattering from valence electrons is much weaker compared with that of the core electrons since only a small number of valence electrons actively participate in bond forming and breaking. Thus, the desired information about chemical reactivity is masked by the much stronger signal coming from an overwhelmingly large number of core electrons. This problem calls for the application of advanced data-processing methods.

Diffraction signals reveal the modulus of the scattering amplitude but not its phase. Reconstruction of the phase is known in crystallography as the phase retrieval problem. The common error-reduction algorithm (7, 8) is based on iterative back and forth Fourier transformations between momentum and coordinate spaces with the inclusion of additional information about the system. Convergence of the phase retrieval algorithms becomes possible due to separation of length scales and sparsity, which often characterize natural objects (9, 10). The same physical properties allow us to develop an effective wavelet-based algorithm for the analysis of the time-evolving electron density.

An approach for imaging and detection of the flow of valence electrons in space and time during a chemical process based on scale separation of X-ray diffraction data was proposed in ref. 11. The molecular electron density $\rho(\boldsymbol{r})$ was partitioned as

$$\rho(\boldsymbol{r}) = \rho_{core}(\boldsymbol{r}) + \rho_{val}(\boldsymbol{r}). \quad [1]$$

The core electron density, ρ_{core}, represents the electrons which occupy the lowest energy levels and dominate the diffraction amplitude. The core electrons are highly localized in the vicinity of their respective nuclei. According to the Heisenberg uncertainty relation this leads to a broad distribution in momentum space. The momentum exchange in an elastic scattering process thus results in a wide range scattering angles (i.e., a broad range of $\boldsymbol{k}$ values in reciprocal space). The valence electrons in contrast are more delocalized, which results in a narrow distribution in momentum space. Consequently they are more localized in reciprocal space (i.e., around low $\boldsymbol{k}$ values). A low-pass filtered Fourier transform from $\boldsymbol{k}$ space to coordinate space with the cutoff $|\boldsymbol{k}| < k_{limit}$ was used in ref. 11 to enhance the contribution of ρ_{val} by discriminating against the core electrons. This is a typical image-processing problem (i.e., the ability to recognize objects in an image) combined with the known phase-retrieval algorithm.

In this paper, we develop a wavelet-based algorithm for separating the short- and the long-scale contributions to the electron

Significance

Free electron laser sources of ultrafast X-ray pulses can record movies of chemical reactions by measuring snapshots of the charge density along the reaction path on the femtosecond timescale. Only a few valence electrons typically participate in chemical bond breaking and forming. To separate the valence electron density from the strong background of highly localized core electrons we use a wavelet transform, a powerful tool for filtering, and scaling analysis of signals. The wavelet-processed signal from the cyclohexadiene molecule reported here clearly reveals the valence electron rearrangements in the early steps of the photoinduced pericyclic ring opening reaction, which are not resolved in the bare signal. This multiscale analysis of charge densities should be extremely valuable for disentangling complex reaction pathways.

Author contributions: V.A.O. designed research; S.M. performed research; V.A.O. and M.K. analyzed data; and V.A.O. wrote the paper.

Reviewers: M.I., Max Born Institute; and H.J.W., ETH Zurich.

The authors declare no conflict of interest.

Published under the PNAS license.

[1]V.A.O. and M.K. contributed equally to this work.

[2]To whom correspondence should be addressed. Email: smukamel@uci.edu.

Published online September 25, 2018.

density. The wavelet transform, widely used in multiscale image processing, maps a function $f(x)$ of coordinate x onto a 2D space (s, u) by convolution with a wavelet function $s^{-1/2}\psi\left((x-u)/s\right)$, where s is a dilation parameter and u is a translation of the mother-wavelet function $\psi(x)$. The transform $\mathscr{F}(u, s)$ (4) serves as a mathematical microscope, with an optical system described by convolution with $\psi(x)$, global magnification $1/s$, and optical axis positioned at u. This transformation is exact and reversible (5). By selective targeted filtering of a domain in (s, u) space followed by inverse transformation to x space, we can highlight desired features of the original function $f(x)$. The idea of mapping into a higher-dimensional space is reminiscent of the Wigner transform where a function of x is mapped onto phase space (x, k), which allows filtering in phase space (12). However, unlike the wavelet transform, the Wigner transform is nonlinear and nonreversible. The wavelet transform is thus much more convenient.

Wavelets have been routinely used for improving numerical density-functional theory methods (see chapter 13 in ref. 1). An effective wavelet-based algorithm for peak detection in nanoparticle X-ray diffraction 1D patterns was proposed (13) and later implemented in X-ray absorption spectroscopy (14, 15). It was demonstrated that wavelet processing of 1D spectral data allows one to resolve strongly overlapping Gaussian and Lorentzian peaks (16). Here we implement a wavelet decomposition toward the analysis of snapshot images of electron density transformation during the early stages of the pericyclic photoinduced ring-opening reaction of 1,3-cyclohexadiene (CHD) (1). By separating the core electron patterns in the 2D projection of the electron density we can partition the electron density according to Eq. **1**. We further extend the method of peak detection in 1D data (13) detecting the positions of hydrogens, which is virtually impossible in the bare diffraction signal, since the lightest atoms carry only a small fraction of the density.

In this section, we apply the wavelet transform toward the characterization of three intermediate steps along the ring-opening reaction of path CHD,

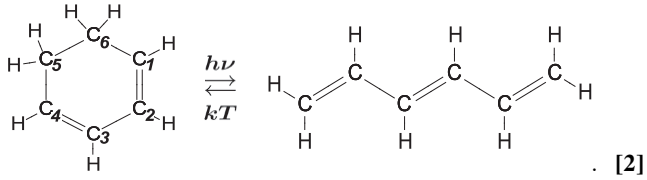

. **[2]**

The CHD ring has six carbon atoms. Atoms C1–C4 participate in the conjugated π-bond system, involving the atomic p orbitals orthogonal to the ring plane. Atoms C5 and C6 enter the $-CH_2-$ groups and have an additional σ bond with a hydrogen atom. Altogether, 12 of the 44 electrons occupy the inner shell (1s) electrons of the carbon atoms, 28 electrons form the σ bonds, and only 4 electrons participate in π bonds. CHD in its ground-state geometry possesses C_2 symmetry; i.e., 180° rotation around the symmetry axis returns the structure into itself (Fig. 1). Excitation with an ~260-nm UV light induces a π–π^* transition, leading to a rearrangement of the π electrons in the ring. This eventually results in breaking of the σ-bond C5–C6 and the formation of hexatriene.

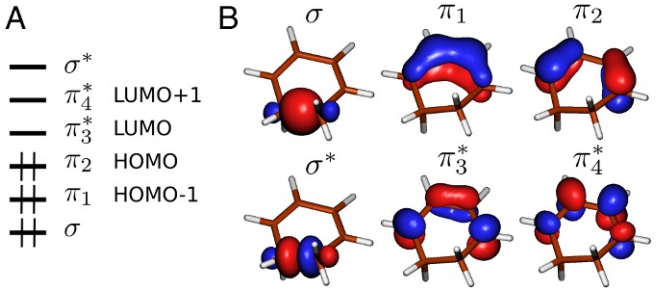

Fig. 1. (*A*) Molecular orbital (MO) occupation scheme for the ground state of the MOs involved in the photochemical reaction. (*B*) Isosurface plots of the MOs (iso value 0.08) shown in *A*.

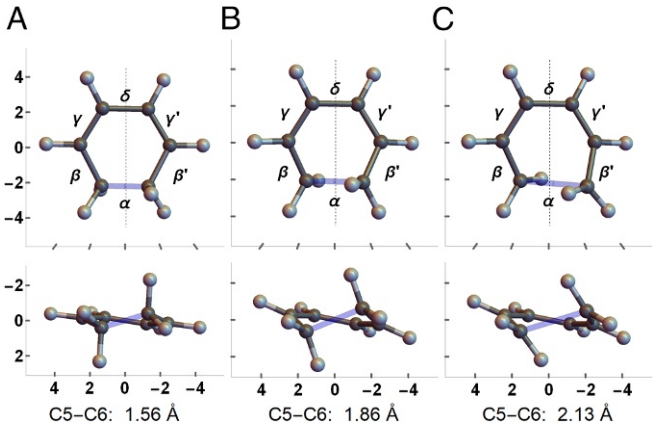

Fig. 2. Three structures (*A*–*C*) of CHD with different lengths of C5–C6 bond (highlighted in blue). The dashed line marks the C_2 symmetry axis. Here and in all of the figures *x* and *y* coordinates are given in atomic units of length (1 Bohr ≈ 0.53 Å).

Reaction **2** is a typical example of an electrocyclic reaction that involves cyclic rearrangements of π and σ bonds and follows the Woodward–Hoffmann σ–π interaction rule. It has been studied in great detail both experimentally and theoretically (reviews in refs. 17 and 18 and references therein). In the photoinduced flow of reaction **2**, upon photoexcitation to S_2, the molecule proceeds through a cascade of structural and electronic rearrangements mediated by two conical intersections (CIs): S_1/S_2 and S_0/S_1. Below we study the electron density distribution at the Franck–Condon point, at the S_1/S_2 CI, and at the step after the S_1/S_2 CI. To that end, we selected the three structures in Fig. 2 *A*–*C* and calculated the electron densities in states S_0, S_1, and S_2 for each of them. Structure *A* is the equilibrium ground-state geometry. Structure *B* is the geometry of the CI between S_2 and S_1, which has an elongated C5–C6 bond. In structure *C*, we elongated the C5–C6 bond farther, by 0.3 Å, and broke the C_2 symmetry to emphasize the electronic rearrangement toward hexatriene. The electronic configurations and the corresponding charge densities were calculated with the program package MOLPRO (19) at the complete active space self-consistent field (CASSCF)(6/6)/6-31G* level of theory. The active space includes the σ/σ^* orbitals of the C5–C6 single bond and the π/π^* orbitals of the conjugated double bonds (Fig. 1). Structure *A* was obtained by optimizing the geometry of the S_0 state. Structure *B*, which corresponds to the geometry of the S_1/S_2 CI, was generated by geometry optimization in the CI vicinity starting from S_0 geometry. Structure *C* was created by elongating the bond distance C5–C6 in structure *B* to 2.13 Å.

Using a wavelet transform we separated the core electron density from the valence electron density and pinpointed the positions of protons as explained in *Methods: Wavelet Decomposition*. This resolution allows us to clarify the nature of valence electron density and distinguish single and double bonds, as is shown below. The bare and the wavelet-processed electron densities for all structures are presented in Fig. 3 for the electronic state S_0, in Fig. 4 for S_1, and in Fig. 5 for S_2.

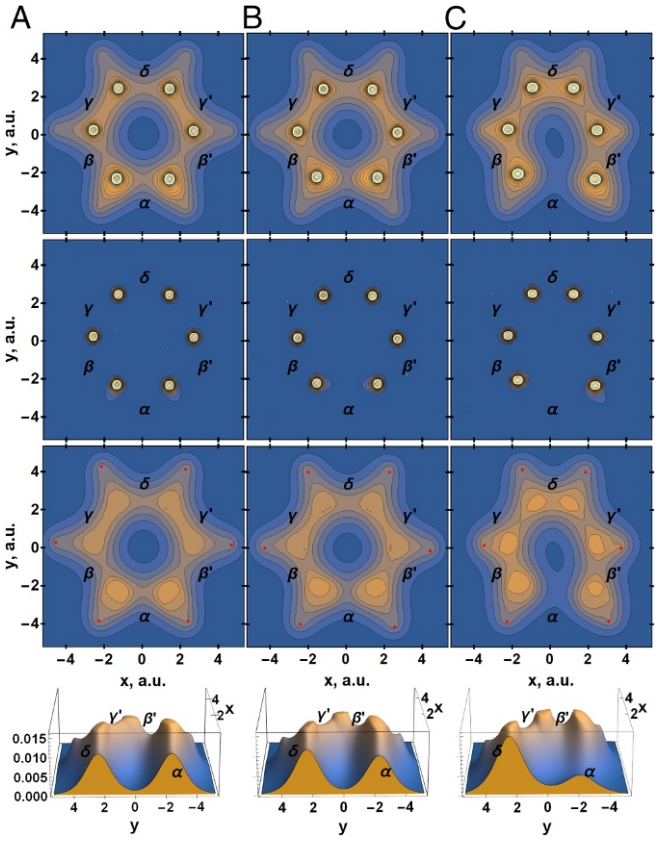

Fig. 3. Processing of CHD electron densities in state S_0 for structures *A*, *B*, and *C*. First row shows 2D projection of the total electron density before processing, second row shows the core electron density, and third row shows the valence electron density. Red dots mark the hydrogen atoms, and the highlighted bonds of structures in Fig. 2 correspond to features α. Fourth row shows valence electron density surface plot sectioned along the C_2 symmetry axis. The maximal values of the electron density calculated on the interatom spaces are given in Table 1.

Results

The Bare and Wavelet-Processed Electron Density Distributions

We analyze the decomposed densities, Eq. **1**, at all three nuclear configurations *A*, *B*, and *C* for the three electronic states S_0, S_1, S_2 (Figs. 3–5). The snapshot images of the density are discussed on the CASSCF model surfaces in the order the photochemical reaction would take place: The initial state is S_0, structure *A*. A vertical excitation with UV light brings the molecule into the state S_2, structure *A*. From there it evolves toward the CI (structure *B*) and crosses over to S_1. Finally the C5–C6 bond is broken and the all cis-hexatriene is represented by structure *C*.

The *A* Structure. We begin with the CHD ground state at its equilibrium geometry. Fig. 6*A* shows the 2D projection of the density on the (x, y) (carbon-ring) plane, where the sharp peaks from the carbon 1s core electrons are visible. The wavelet decomposition of the 2D projection splits the projection onto sharp (Fig. 6*B*) and smooth (Fig. 6*C*) parts (also Fig. 3, column *A*). Fig. 3 *A*–*C*, second row shows the retrieved densities of the carbon 1s core electrons, which can be interpreted as the approximate positions of the carbon nuclei. The retrieved valence electron density in Fig. 3 *A*–*C*, third row contains all electrons that make up the σ and π bonds. This also includes the hydrogen atoms marked by red dots, whose positions can be located by using the searching algorithm discussed in *Methods: Wavelet Decomposition*. The electron density of the conjugated π system can be rationalized by examining the occupied and unoccupied molecular orbitals. In the ground state the highest occupied molecular orbital (HOMO) and HOMO-1 are doubly occupied, as shown in Fig. 1. Summing up the charge density of those two molecular orbitals maximizes the density at γ and γ', as is clearly visible in Fig. 3 *A*–*C*, third row. The density value at the central point of the γ line is $\sim 4.85 \times 10^{-2}$[e/Å^2]. It is the highest value compared with other segments (Table 1). This resembles the Lewis structure of CHD. Looking at the cut through δ and α (Fig. 3 *A*–*C*, fourth row), one can clearly see that the charge densities in δ and α are nearly identical and both have a single-bonding character.

We next examine the S_2 excited state, which corresponds to a vertical excitation of CHD with UV light. Fig. 5 shows the charge densities of the S_2 state and the corresponding wavelet decomposed charge densities. While the core electron charge density (Fig. 5 *A*–*C*, second row), is still identical to that of Fig. 3 *A*–*C*, second row, the valence electron density in Fig. 3 *A*–*C*, third row is visibly different now. The electron density in γ/γ' (for numerical values see Table 1) is slightly decreased and increased in δ. This increased delocalization of the charge density in the conjugated π system can be explained by the electron configuration: The S_2 state is dominated by the HOMO-LUMO (lowest unoccupied molecular orbital) excitation, which relocates charge density to δ.

The *B* Structure. In the photochemical reaction the electronically excited CHD evolves toward the CI on the S_2 potential energy surface. A snapshot of the geometry at the CI is represented by structure *B*. The nuclear geometry change can now be extracted from the core electron density in Fig. 5 *A*–*C*, second

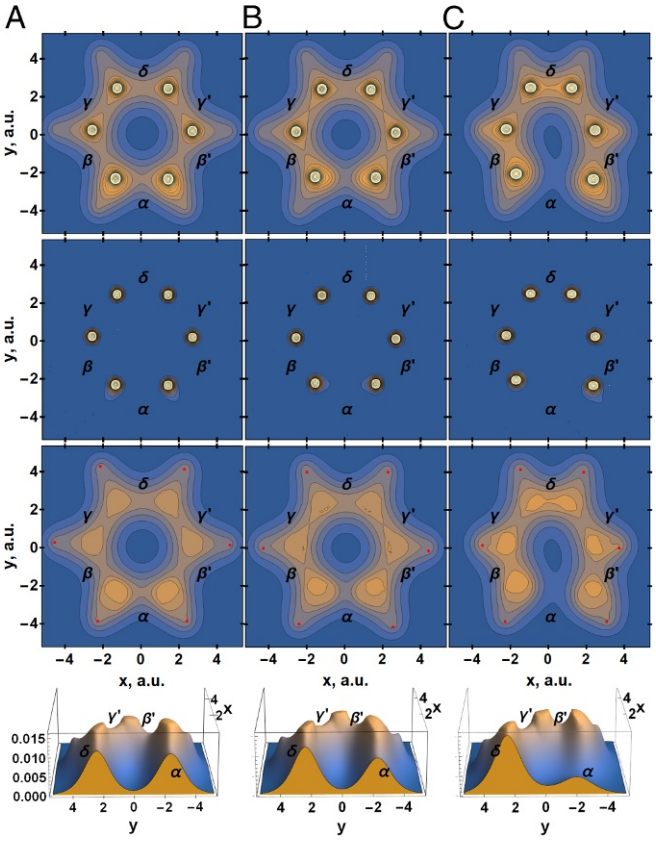

Fig. 4. Same as Fig. 3 but for the S_1 state.

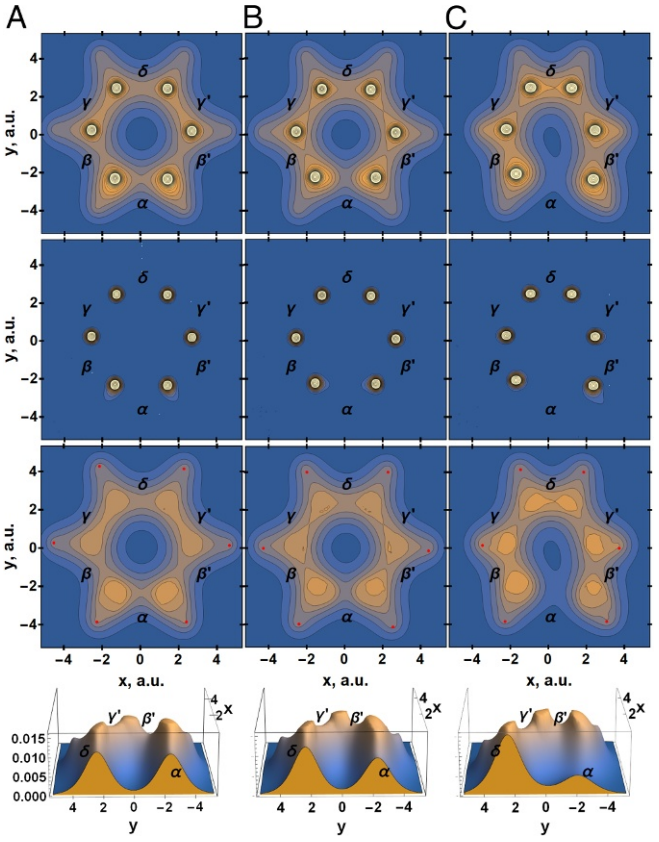

Fig. 5. Same as Fig. 3 but for the S_2 state.

row. The valence electron charge densities of the S_1 (Fig. 4 *A–C*, third row) and S_2 states (Fig. 5 *A–C*, third row) are now converged and show no visible difference (their eigenvalues/energies are degenerate at this point). However, comparing the electron densities with structure *A* (Franck–Condon point, Fig. 5), the onset of the C5–C6 bond breaking becomes visible. Inspection of the density at region α shows a clear decrease (Fig. 5 *A–C*, fourth row, and Table 1), indicating a weakening of the bond. The density of the conjugated π system is now uniformly distributed over β, γ, δ, γ', and β'. This indicates the preformation of the hexatriene form (i.e., the formation of three conjugated double bonds).

The *C* Structure. Structure *C* represents the open ring form. The C_2 symmetry is now broken and γ/γ' and β/β' are no longer perfectly symmetric. Looking at the S_1 state in Fig. 4 *A–C*, third and fourth rows, one can clearly see that the C5–C6 at α is now broken and the three alternating double bonds are now nearly in place at β, δ, and β'.

To assess the quality of the density separation one can use the integration over each part to recover the electrons numbers (Table 1). The wavelet transform gives 11.3 and 11.1 core electrons (12 carbon 1s are expected), which is a 6% and 8% difference in the number of electrons. This is an approximate 1% difference per C atom. This mismatch is due to the wavelet transform and to the fact that the charge density is represented on a numerical grid (imperfect input to the wavelet transform).

Conclusions

We implemented the wavelet transform protocol toward the analysis and dissection of electron densities in the photoinduced electrocyclic reaction of ring opening in CHD. The method uses large differences in length scales to separate contributions of core and valence electrons. Snapshots at various positions along the quantum reaction path were examined. We demonstrated that the method can yield a high-resolution picture of the electron density features and even allows one to distinguish the weak electron density localized around hydrogen atoms. The resolution offered by the wavelet algorithm can be demonstrated from estimation of the number of electrons participating in smooth and sharp (total number is 12) parts of the electron density (Table 1).

The present method can be improved further. In particular, the algorithm for separation of wavelet coefficients uses the criterion of nullification of coefficients on the domain borders. Instead, one can implement an interpolation of points in the vicinity of domain boundaries to make the smooth part of the density even smoother. We applied the method for the analysis of a small planar 2D molecule in various electronic states, the natural extension of the approach to 3D electron densities. Because of higher dimensionality of the target space, the 3D density processing must be based on quantitative analysis algorithms rather than visualization. The combination of wavelets with phase retrieval algorithms could facilitate the multiscale analysis of X-ray signals.

Besides time-resolved X-ray spectroscopy, wavelets can be applied to conventional optical spectroscopy to reveal hidden structures, like peaks and time evolution in 2D spectra, or make a smart compression algorithm for large spectroscopic datasets.

Methods

Wavelet Decomposition To separate core and valence electron contributions to the electron density we used a 2D continuous-wavelet transform (CWT) with LoG mother wavelet (20, 21),

$$\psi(\boldsymbol{x}) = \left(\frac{|\boldsymbol{x}|^2}{2} - 1\right) e^{-|\boldsymbol{x}|^2/2}; \quad \tilde{\psi}(\boldsymbol{k}) = -|\boldsymbol{k}|^2 e^{-|\boldsymbol{k}|^2/2}. \qquad [3]$$

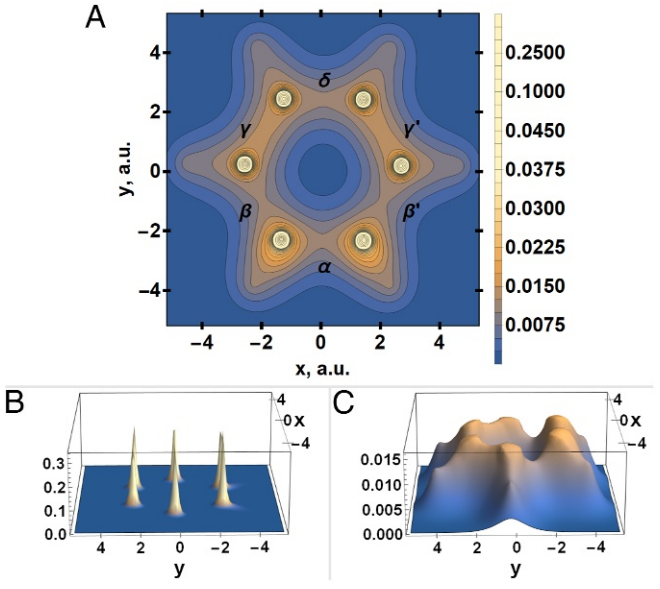

Fig. 6. (*A*) A 2D projection of the electron density on the carbon-ring plane. The density is measured in units [e/Å^2] and the integral is normalized on 44 electrons, the total number of electrons. (*B*) Surface plot of the sharp part of electron density restored by using wavelet transform. It is associated with the core electron density. (*C*) Smooth part of the electron density restored by using wavelet transform. The color scheme and coordinate are the same for this and all other density plots in the text.

Table 1. Quantitative estimations of electron density features

State, geometry	α	β	γ	δ	Core	Valence
S_0, *A*	3.42	3.85	4.85	3.75	11.3	32.7
S_1, *A*	3.42	4.00	4.41	4.04	11.3	32.7
S_2, *A*	3.38	3.93	4.63	3.94	11.3	32.7
S_0, *B*	3.21	4.42	4.64	4.06	11.1	32.9
S_1, *B*	3.01	4.54	4.50	4.25	11.1	32.9
S_2, *B*	3.01	4.54	4.51	4.25	11.1	32.9
S_0, *C*	1.28	4.81	4.44	5.24	11.3	32.7
S_1, *C*	1.14	4.91	4.34	5.38	11.3	32.7
S_2, *C*	1.24	4.81	4.40	5.37	11.3	32.7

The columns α, β, γ, δ contain values of electron density (in units $\times 10^{-2}$[e/Å^2]) calculated at the saddle points on the corresponding arcs. In the columns "Core" and "Valence" estimation of the number of electrons entering the core and valence density parts (totally 44 electrons) are given.

The wavelet Eq. **3** is an isotropic function, i.e., independent on the coordinate plane rotation (Fig. 7*D*). The CWT can be defined in both $\boldsymbol{x}$ and $\boldsymbol{k}$ spaces by (22)

$$\begin{aligned}\mathcal{F}(s,\boldsymbol{u}) &= s^{-1}\int_{\mathbb{R}^2} d^2\boldsymbol{x}\, f(\boldsymbol{x})\psi\left[s^{-1}(\boldsymbol{x}-\boldsymbol{u})\right]\\ &= s\int_{\mathbb{R}^2} d^2\boldsymbol{k}\,\tilde{f}(\boldsymbol{k})\tilde{\psi}\left[s\boldsymbol{k}\right]e^{i\boldsymbol{u}\boldsymbol{k}},\end{aligned} \qquad [4]$$

where $\tilde{f}$ denotes Fourier transform of function f. The inverse transform is given by

$$f(\boldsymbol{x}) = C_\psi^{-1}\int_{\mathbb{R}^2\times\mathbb{R}_+}\mathcal{F}(s,\boldsymbol{u})\psi\left[s^{-1}(\boldsymbol{x}-\boldsymbol{u})\right]d^2\boldsymbol{u}\frac{ds}{s^3}d\theta, \qquad [5]$$

provided the admissibility constant $C_\psi = \int_{\mathbb{R}^2}\left|\tilde{\psi}\left[\boldsymbol{k}\right]/\left|\boldsymbol{k}\right|\right|d\boldsymbol{k}$ is finite. This condition reflects the zero mean property of wavelet, $\int d^2\boldsymbol{x}\psi(\boldsymbol{x}) = 0$.

The parameter space of a generic 2D wavelet transform (22) consists of the coordinates $(s,\theta,\boldsymbol{u})$. s and θ play the role of spatial frequency, i.e., momentum in polar coordinates, so that the full 4D parameter space constitutes our phase space. Computations of 2D CWT with isotropic wavelets, when the phase space becomes effectively 3D with a dummy variable θ, allows us to reduce the data size. As an example, we display in Fig. 7*A* wavelet transform $\mathcal{F}(s,\boldsymbol{u})$ of the 2D electron density of Fig. 6*A*. The region of $(s,\boldsymbol{u})$ space, which is essential for our numerical investigation, is a rectangular parallelepiped. Its cross-section parallel to the $(u_x u_y)$ plane has a square shape. For small scales, $s \lesssim 2^2$, the nonzero values of $\mathcal{F}(s,\boldsymbol{u})$ are concentrated around the positions of nuclei, since integration of the shrink wavelet with the smooth part of distribution gives zero due to the admissibility condition. At large s, $s \gtrsim 2^5$, the sharp features do not contribute to the integral because of the large $1/\sqrt{s}$ and the nonzero coefficients appear in a single blob. $\mathcal{F}(s,\boldsymbol{u})$ vanishes either asymptotically when $\boldsymbol{u}\to\infty$ or $\log_2 s \to \pm\infty$ or at the boundaries, when the density changes its behavior. In the latter case nullification of coefficients indicates presence of discontinuities of the density at a certain scale s. We use this property to find the borders of domains in $(s,\boldsymbol{u})$ space and separate them from each other.

The core electron density is strongly localized around carbon atoms, which means that it generates well-distinguished domains of high amplitudes of $\mathcal{F}(s,\boldsymbol{u})$ in $(s,\boldsymbol{u})$ space. For very small s $(s<2^0)$ the domains are stretched isotropically (due to circular symmetry of core electron density) around six carbon atom positions, $\boldsymbol{u}_i$ $(i=1,\ldots,6)$. At given s the condition $\mathcal{F}(s,\boldsymbol{u}_i+\delta\boldsymbol{u})\le 0$ allows one to determine the border of the ith domain. The procedure is continued until the region of intermediate scales $s\sim 2^4$. Due to linearity of the wavelet transform, one can make the inverse transform for each of six domains separately. This allows one to find contributions to the sharp part of electron density, which is associated with the core electrons.

The difference in scales also allows one to detect algorithmically positions of atoms. This is an extension of the method proposed in ref. 13 for peak detection in 1D datasets: The minima of $\mathcal{F}(s,\boldsymbol{u})$ at given scales ($s\sim 2^{-2}$ for carbon and $s\sim 2^1$ for hydrogen) point out positions of maxima of the original density function (Fig. 7 *B* and *C*). The density around hydrogen atoms is weak and hard to distinguish from background. To detect hydrogens we use information about curvature of the density surface rather than absolute values of density. The density grows with the scale $s_h\sim 2^1$ and has a maximum at coordinates of the proton. This feature manifests itself in amplitudes of $\mathcal{F}(s_h,\boldsymbol{u})$, which makes it easy to detect. Note that some other extreme points of electron density can have the same length scales. They also appear as anisotropic shape minima of function $\mathcal{F}(s_h,\boldsymbol{u})$ (Fig. 7*C*). Atoms with different numbers of core electrons can be distinguished by their fingerprints at various scales s in a similar way.

Our simulation protocol is summarized as follows:

i) Calculation of 2D CWT of the electron density projection using Eq. **4**.
ii) Localization of local minima of the function $\mathcal{F}(2^{-2},\boldsymbol{u})$ to find the positions $\boldsymbol{u}_i$ $(i=1,\ldots,6)$ of six carbon atoms.
iii) Separation of domains in $(s,\boldsymbol{u})$ space: The ith small domain includes all points $(s,\boldsymbol{u}_i+\delta\boldsymbol{u})$ around the ith carbon atom center $\boldsymbol{u}_i$ at $s<2^4$, such that $\mathcal{F}(s,\boldsymbol{u}_i+\delta\boldsymbol{u})\le 0$. The largest domain (corresponding to the smooth part of density) is the complement to the union of all small domains.

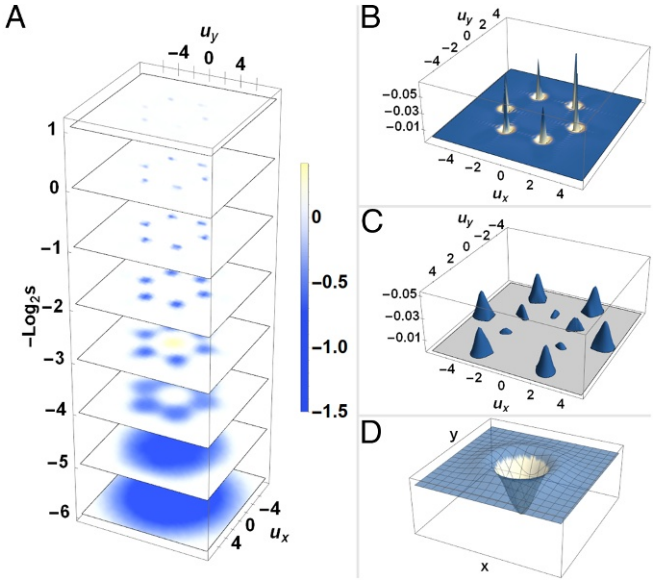

Fig. 7. (*A*) Wavelet transform $\mathcal{F}(s,\boldsymbol{u})$ of the 2D electron density of Fig. 6*A* with LoG wavelet **3**. (*B*) A 3D plot of the $\mathcal{F}(2^{-2},\boldsymbol{u})$ surface. The peaks correspond to positions of carbon atoms. (*C*) A 3D plot of negative values of $\mathcal{F}(2^1,\boldsymbol{u})$. The peaks generated by carbon atoms are screened so that peaks from hydrogen atoms and anisotropic peaks from local extremes of valence electron density become visible. (*D*) Plot of LoG mother wavelet (Mexican hat), Eq. **3**.

CHEMISTRY

iv) Detection of hydrogen atom positions and extreme points on the density surface by finding local minima of $\mathcal{F}(2^1, \boldsymbol{u})$ (excluding those at $\boldsymbol{u}_i,\ i = 1, \ldots, 6$). Isotropic minima correspond to positions of hydrogens, and anisotropic minima correspond to other extremal features of the electron density.

v) To obtain the smooth and sharp parts of electron density the inverse CWT is calculated by Eq. **5** for each domain defined in step *iii* separately.

Wavelet analysis of the electron densities was based on methods included in the Wavelet Toolbox of Matlab and the Wavelet transform package provided by Wolfram Mathematica.

ACKNOWLEDGMENTS. This work was supported by the US Department of Energy (DOE), Office of Science, and Basic Energy Sciences under Award DE-FG02-04ER15571 and by the National Science Foundation (Grant CHE-1663822). M.K. was also supported by a DOE grant.

1. Roy AK, ed (2012) *Theoretical and Computational Developments in Modern Density Functional Theory, Physics Research and Technology* (Nova Science Publishers, New York).
2. Runge E, Gross EKU (1984) Density-functional theory for time-dependent systems. *Phys Rev Lett* 52:997–1000.
3. Milne C, Penfold T, Chergui M (2014) Recent experimental and theoretical developments in time-resolved x-ray spectroscopies. *Coord Chem Rev* 277–278:44–68.
4. Minitti MP, et al. (2015) Imaging molecular motion: Femtosecond x-ray scattering of an electrocyclic chemical reaction. *Phys Rev Lett* 114:255501.
5. Ki H, Oang KY, Kim J, Ihee H (2017) Ultrafast x-ray crystallography and liquidography. *Annu Rev Phys Chem* 68:473–497.
6. Bennett K, Kowalewski M, Rouxel JR, Mukamel S (2018) Monitoring molecular nonadiabatic dynamics with femtosecond X-ray diffraction. *Proc Natl Acad Sci USA* 115:6538–6547.
7. Gerchberg RW, Saxton WO (1972) A practical algorithm for the determination of the phase from image and diffraction plane pictures. *Optik* 35:237–246.
8. Klibanov MV (2006) On the recovery of a 2-D function from the modulus of its Fourier transform. *J Math Anal Appl* 323:818–843.
9. Marchesini S (2008) Ab initio compressive phase retrieval. arXiv:0809.2006.
10. Netrapalli P, Jain P, Sanghavi S (2013) Phase retrieval using alternating minimization. *Proceedings of the 26th International Conference on Neural Information Processing Systems - NIPS'13*, eds Burges CJC, Bottou L, Welling M, Ghahramani Z, Weinberger KQ (Curran Associates, New York), Vol 2, pp 2796–2804.
11. Bredtmann T, Ivanov M, Dixit G (2014) X-ray imaging of chemically active valence electrons during a pericyclic reaction. *Nat Commun* 5:5589.
12. Schleich WP (2001) *Quantum Optics in Phase Space* (Wiley-VCH, Berlin).
13. Gregoire JM, Dale D, van Dover RB (2011) A wavelet transform algorithm for peak detection and application to powder x-ray diffraction data. *Rev Sci Instrum* 82:015105.
14. Penfold TJ, et al. (2013) A wavelet analysis for the x-ray absorption spectra of molecules. *J Chem Phys* 138:014104.
15. El Nahhas A, et al. (2013) X-ray absorption spectroscopy of ground and excited rhenium–carbonyl–diimine complexes: Evidence for a two-center electron transfer. *J Phys Chem A* 117:361–369.
16. Xiaoquan L, Hongde L, Zhonghua X, Qiang Z (2004) Maximum spectrum of continuous wavelet transform and its application in resolving an overlapped signal. *J Chem Inf Comp Sci* 44:1228–1237.
17. Deb S, Weber PM (2011) The ultrafast pathway of photon-induced electrocyclic ring-opening reactions: The case of 1,3-cyclohexadiene. *Annu Rev Phys Chem* 62: 19–39.
18. Arruda BC, Sension RJ (2014) Ultrafast polyene dynamics: The ring opening of 1,3-cyclohexadiene derivatives. *Phys Chem Chem Phys* 16:4439–4455.
19. Werner HJ, et al. (2015) *Molpro, Version 2015.1, a Package of ab Initio Programs*. Available at https://www.molpro.net. Accessed August 3, 2018.
20. Daubechies I (1992) *Ten Lectures on Wavelets* (Society for Industrial and Applied Mathematics, Philadelphia).
21. Cohen J, Zayed AI (2011) *Wavelets and Multiscale Analysis, Theory and Applications* (Birkhäuser, Boston).
22. Antoine JP, Carrette P, Murenzi R, Piette B (1993) Image analysis with two-dimensional continuous wavelet transform. *Signal Process* 31:241–272.